Hindawi Publishing Corporation
EURASIP Journal on Wireless Communications and Networking
Volume 2008, Article ID 248509, 11 pages
doi:10.1155/2008/248509

Research Article

A Comprehensive Evaluation of Joint Range and Angle Estimation in Indoor Ultrawideband Location Systems

Camillo Gentile, A. Judson Braga, and Alfred Kik

Wireless Communication Technologies Group, National Institute of Standards and Technology, Gaithersburg, MD 20899, USA

Correspondence should be addressed to Camillo Gentile, camillo.gentile@nist.gov

Received 17 December 2007; Revised 2 June 2008; Accepted 18 September 2008

Recommended by Richard Kozick

Fine time resolution enables ultrawideband (UWB) ranging systems to extract the first multipath arrival corresponding to the range between a transmitter and receiver, even when attenuated in strength compared to later arrivals. Bearing systems alone lack any notion of time and in general select the strongest arrival which is rarely the first one in nonline-of-sight conditions. Complementing UWB ranging systems with bearing capabilities allows indexing the arrivals as a function of both time and angle in order to isolate the first, providing precision range and angle. However, that precision degrades with the increasing presence of walls and other objects which distort the properties of the first arrival. In order to gauge the physical limits of the joint UWB system, we design and assemble a spatial-temporal channel sounder using a vector network analyzer coupled to a virtual antenna array, and conduct 200 experiments to measure the time- and angle-of-flight. The experiments are carried out in both line-of-sight and nonline-of-sight conditions up to an unprecedented 45 meters throughout four separate buildings with dominant wall material varying from sheet rock to steel. In addition, we report performance for varying bandwidth and center frequency of the system. We find that operating at a bandwidth of 4 GHz suffices in resolving multipath in most buildings and in excess shows virtually no improvement. While the range error decreases at lower center frequencies, the higher frequencies offer better angular resolution and so smaller angle error.

1. INTRODUCTION

Location systems with ranging capabilities alone necessitate at least three base stations with known locations to extract the two-dimensional position of an unknown device through triangulation [1]. In emergency operations such as fire rescue, no such infrastructure exists to date as part of the building code, nor does time permit installation as a crisis unravels. However, if both the range and the angle of the device were known, then a single-base station alone could extract its location. Moreover, if the base station itself were a mobile device attached to a fireman, then the system could be used to find trapped victims equipped with beacon tags, yielding their locations with respect to the fireman as he moves about.

Ultrawideband (UWB) technology is characterized by a bandwidth greater than 500 MHz or exceeding 20% of the center frequency of radiation [2]. Its fine time resolution and the presence of lower frequencies in the signal to penetrate walls enable UWB ranging systems to extract the first multipath arrival corresponding to the range between a transmitter and receiver, even when attenuated in strength compared to later arrivals. Bearing systems alone lack any notion of time and in general select the strongest arrival which is rarely the first one in nonline-of-sight conditions. Complementing UWB ranging systems with bearing capabilities allows indexing the arrivals as a function of both time and angle in order to isolate the first, providing precision range and angle. While in principle boosting transmission power to levels above the FCC mask can ensure connectivity for large buildings, connectivity alone cannot guarantee precision due to the distorting effects of walls (and other objects) in the direct path. The number of wall interactions in general increases with range, leading to a degradation in precision due to the physical limits of the system. The large dynamic range of our system allows us to quantify this degradation up to an unprecedented 45 meters in our evaluation.

Irahhauten et al. provides a comprehensive overview of the ultrawideband channel propagation measurements taken in recent years to model the *temporal* properties of the indoor channel [3]. Amongst those properties, only Lee and Scholtz [4] and Denis et al. [5] report the statistics on the *time-of-flight* besides us. The comprehensive measurement campaign in our previous work [6] shows that UWB technology can deliver ranging precision from a few centimeters to a tens of centimeters based on the operating conditions. Surprisingly, there has been very little effort to model the *spatial* properties of the UWB channel [7–11], but even these papers lack statistics on the angle of the first arrival, of particular interest in location systems. Analogous to our comprehensive evaluation of the time-of-flight for UWB ranging, we extend the measurement suite to include *angle-of-flight* as well, and show its performance according to variation in system parameters. Specifically, the main contribution of this paper is a study of how the angle error, range error, and their joint location error change with respect to

(i) *bandwidth*: precision increases with bandwidth, but carries diminishing returns with the additional expense;

(ii) *center frequency*: lower frequencies penetrate materials better, but higher frequencies offer better angular resolution;

(iii) *construction material*: compare performance with typical building construction materials varying as sheet rock (easy), plaster, cinder block, to steel (most difficult), to gauge lower and upper bounds on the technology rather than with building layout (i.e., office, residential typically have the same wall materials);

(iv) *long range*: the high dynamic range of our system allows us to span 45 meters and examine the limits in the technology inherent to the interaction with up to 10 walls.

The paper reads as follows. Section 2 introduces the temporal indoor channel propagation model and describes our ultrawideband system to measure its properties. Incorporating a uniform circular array into the system in Section 3 enables characterizing the joint spatial-temporal properties of the channel from which the time and angle-of-flight can be extracted, as explained in Section 4. Section 5 provides the details of our equipment setup and Section 6 outlines our suite of measurements, presenting results both through statistical metrics and in graphical format, followed by conclusions in the last section.

2. THE TEMPORAL INDOOR PROPAGATION CHANNEL

The traditional model for the indoor propagation channel is an *impulse response* composed from K multipath arrivals indexed through k [12]:

$$h(t) = \sum_{k=0}^{K-1} \alpha_k \delta(t - \tau_k), \tag{1}$$

where τ_k denotes the delay of the arrival in propagating between the transmitter and the receiver and α_k denotes the complex-valued amplitude which accounts for both attenuation and phase change due to reflection, diffraction, and other specular effects introduced by walls (and other objects) on its path. Ranging systems based on time-of-flight estimate the delay τ_0 associated with the arrival of the first impulse in the response, or *leading edge*. Since the signal propagates at the speed of light c in free space, the estimated range between the radios is $c \cdot \tau_0$. Indoor propagation delivers many and closely packed arrivals to the receiver inherent to the smaller dimensions of objects compared to outdoors. Ultrawideband transmitters send pulses sufficiently narrow in time to allow for path discrimination at the receiver, avoiding overlap of the pulses which may otherwise combine in a destructive manner and render poor results. Even though UWB can isolate multipath arrivals, the interaction with the walls distorts the signal. The leading-edge path propagating through walls is usually attenuated with respect to another reflected path, or even buried below the noise floor of the channel. Even if detectable, the leading edge propagates through walls slower than the speed of light, adding an irrecoverable delay with each in the estimation of τ_0 since the numbers of walls and construction material are unknown a priori. Sheet rock (cinder block) introduces an additional delay of 1.8 ns/m wall (3.4 ns/m wall) for a total range error of 54 cm (102 cm) through 10 walls typically 10 cm thick [13]. Besides the irrecoverable delay, each interaction can also deflect the leading edge off its original trajectory angle. These phenomena place a physical limit on the performance of the system.

The impulse response of the channel in (1) has a *frequency response*

$$H(f) = \sum_{k=0}^{K-1} \alpha_k e^{-j2\pi f \tau_k}, \tag{2}$$

suggesting that the channel can be characterized using *frequency diversity*. We compute $H(f) = Y(f)/X(f)$ by transmitting tones $X(f)$ with unit amplitude and zero phase across the channel at discrete values of f and then measuring $Y(f)$ at the receiver. Characterizing the channel in the frequency domain offers an important advantage over transmitting a fixed pulse in the time domain and recording the impulse response directly. Once we sweep the 2–8 GHz band of interest, a subband with bandwidth B and the center frequency f_c can be selected a posteriori in varying the parameters of the system. The discrete frequency spectrum $X(f)$ transforms to the time domain as a periodic sinc pulse $x(t)$ with revolution $1/\Delta f$ modulated at f_c [14]. The bandwidth controls the width of the main lobe defined through the first zero-crossing at $\tau_z = 1/B$, and in turn controls the multipath resolution of the system. Choosing $\Delta f = 1.25$ MHz allows for a maximum multipath spread of 800 nanoseconds, which proves sufficient throughout all four buildings for the arrivals to subside within one period and avoid time aliasing. The corresponding impulse response can

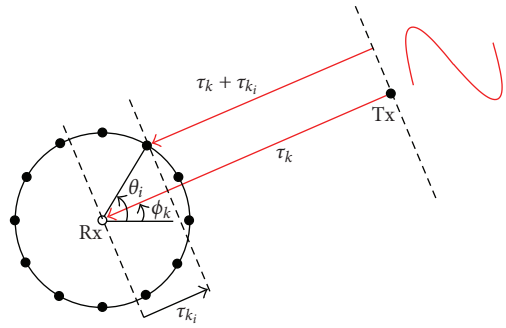

FIGURE 1: The uniform circular array antenna.

be recovered through the inverse discrete Fourier transform (IDFT)

$$h(t) = \sum_{l=0}^{B/\Delta f} H(f) e^{j2\pi f t}, \tag{3}$$

where $f = f_c - B/2 + l \cdot \Delta f$.

3. THE UNIFORM CIRCULAR ARRAY

Replacing the single antenna at the receiver with an antenna array introduces *spatial diversity* into the system. This enables measuring both the temporal and the spatial properties of the UWB channel, in particular the azimuth angle-of-flight ϕ_0 at which the leading edge hits the array at τ_0. For this purpose, we chose to implement the uniform circular array (UCA) over the uniform linear array (ULA) in light of the following two important advantages: (1) the azimuth of the UCA covers 360° in contrast to the 180° of the ULA; (2) the beam pattern of the UCA is uniform around the azimuth angle while that of the ULA broadens as the beam is steered from the boresight.

Consider the diagram in Figure 1 for a single-antenna transmitter and a uniform circular array receiver. The P elements of the UCA are arranged uniformly around its perimeter of radius r, each at angle $\theta_i = 2\pi i/P$, $i = 0 \cdots P-1$. The radius determines the half-power antenna aperture corresponding to $29.2^\circ\, c/r \cdot f$ [15]. Let $H(f)$ be the frequency response of the channel between the transmitter and the reference center of the receiver array. Arrival k approaching from angle ϕ_k hits element i with a delay $\tau_{k_i} = -(r/c)\cos(\phi_k - \theta_i)$ with respect to the center [16], hence the frequency response of each element is a phase-shifted version of $H(f)$, or

$$\begin{aligned} H_i(f) &= H(f) e^{-j2\pi f \tau_{k_i}} \\ &= H(f) e^{j2\pi f (r/c)\cos(\phi_k - \theta_i)}. \end{aligned} \tag{4}$$

In conventional beamforming, the *array frequency response* $H(f,\theta)$ is generated by shifting the phase of each element frequency response $H_i(f)$ into alignment at [16]:

$$H(f,\theta) = \frac{1}{P}\sum_{i=0}^{P-1} H_i(f) e^{-j2\pi f (r/c)\cos(\theta - \theta_i).} \tag{5}$$

A peak occurs in the beam pattern for $\theta = \phi_k$, however the frequency-dependent phase shift in turn generates sidelobes which vary according to the frequency of operation. Figure 2(a) illustrates the different beam patterns of the array response centered at $\theta = 180^\circ$ for $f = 2$ GHz and $f = 8$ GHz.

3.1. Frequency-invariant beamforming

In narrowband systems, numerous filtering techniques [16–18] exist to shape the beam pattern of the array frequency response by applying complex weights to the terms in (5). In wideband systems such as ours, these techniques could be employed, but would require designing separate filters for each subband; even so, it would be difficult to achieve the same beam pattern across the whole band with a finite number of elements. *Frequency-invariant beamformers* can achieve a set beam pattern over a wide frequency band of operation. This class of filters has existed over a decade for uniform linear arrays, but have recently been adapted to uniform circular arrays. They have found application primarily in directional filtering and angle-of-flight estimation [19–21], but to our knowledge, we are the first to employ them in joint time and angle-of-flight estimation.

The development of the frequency-invariant beamformer for the uniform circular array hinges on the expansion

$$e^{j\beta\cos\gamma} = \sum_{n=-\infty}^{\infty} j^n J_n(\beta) e^{jn\gamma}, \tag{6}$$

which when applied to (4) enables separating the phase of the element frequency response into frequency-dependent and independent components:

$$H_i(f) = H(f) \sum_{n=-\infty}^{\infty} j^n J_n\left(2\pi f \frac{r}{c}\right) e^{jn(\phi_k - \theta_i).} \tag{7}$$

The angle ϕ can then be extracted from the above expression by introducing basis functions $e^{jm\theta_i}$ known as *phase modes* (or modes) as in the sequel

$$\hat{H}_m(f) = \frac{1}{P}\sum_{i=0}^{P-1} H_i(f)\cdot G_m(f) e^{jm\theta_i} \tag{8a}$$

$$\begin{aligned} &= H(f) \sum_{n=-\infty}^{\infty} j^n J_n\left(2\pi f \frac{r}{c}\right) e^{jn\phi_k} \\ &\quad \cdot G_m(f)\left[\frac{1}{P}\sum_{i=0}^{P-1} e^{-j(n-m)(2\pi i/P)}\right] \end{aligned} \tag{8b}$$

$$\approx H(f)\cdot j^m J_m\left(2\pi f \frac{r}{c}\right) e^{jm\phi_k} \cdot G_m(f) \tag{8c}$$

$$\approx H(f)\cdot e^{jm\phi_k}. \tag{8d}$$

Transform the element frequency response into the *mode frequency response* $\hat{H}_m(f)$ in (8a) by multiplying each $H_i(f)$ by the mth mode weighted by $G_m(f)$. Substitute (7) into the expression and rearrange as in (8b). Note that the bracketed term is equal to 1 for $n = m + P\cdot z$, $z \in \mathcal{Z}$, and 0 otherwise,

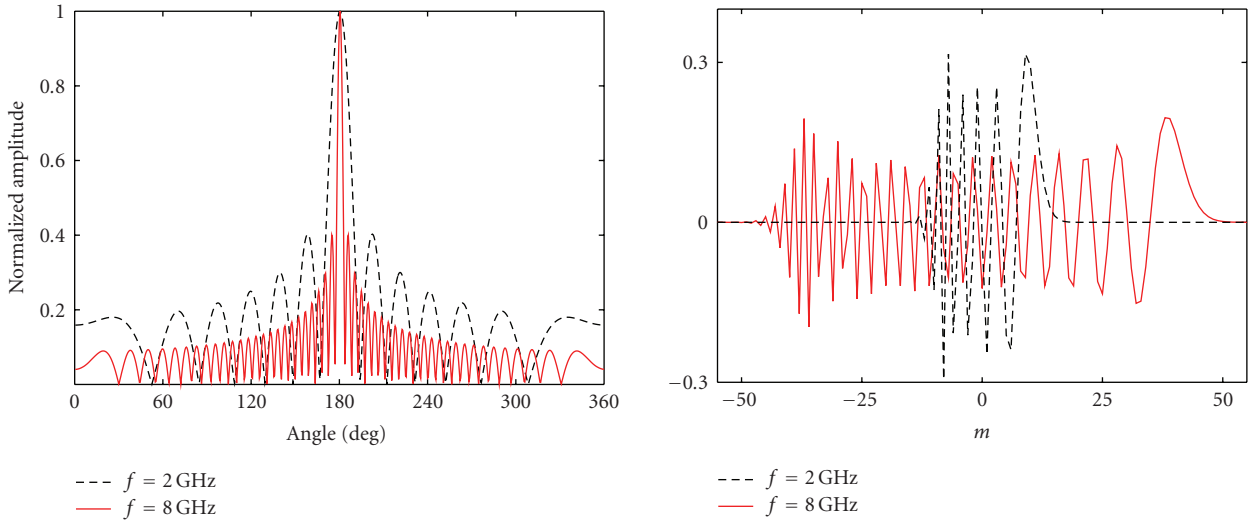

(a) The conventional beamformer

(b) The Bessel functions

Figure 2: The array frequency response at different frequencies.

limiting the values of n in the sum. From [21], the Bessel function has the following property:

$$\left|J_{|n|}\left(2\pi f\frac{r}{c}\right)\right| \leq \left(\frac{2\pi f(r/c)e}{2|n|}\right)^{|n|}, \tag{9}$$

so there exists a number of elements P sufficiently large such that $|J_{|n|}(2\pi f(r/c))| \approx 0$ for $|n| > (P-1)/2$; but the latter condition is always met except for $z = 0$, so the Bessel function in turn is approximately zero except for $n = m$, limiting further the values of n and simplifying (8b) to (8c). By selecting $G_m(f) = 1/j^m J_m(2\pi f(r/c))$, the expression for the mode frequency response simplifies further to (8d).

The Vandermonde structure [22] of the mode frequency response in (8d) in terms of m makes it amenable to the IDFT as a means to recover the frequency-invariant array impulse response by transforming $\hat{H}_m(f)$ from the mode domain to the angle domain $\hat{H}(f,\theta)$:

$$\begin{aligned}\hat{H}(f,\theta) &= \sum_{m=-\infty}^{\infty} \hat{H}_m(f)e^{jm\theta} \\ &= H(f)\cdot \sum_{m=-(P-1)/2}^{(P-1)/2} e^{jm(\theta+\phi_k)}.\end{aligned} \tag{10}$$

As explained previously, $|J_{|m|}(2\pi f(r/c))| \approx 0$ (and in turn $G_m(f)$ in (8c) approaches ∞) for $|m| > (P-1)/2$, so we include only P modes in the Fourier sum above to avoid numerical instability. Figure 2(b) displays the Bessel functions for $f = 2$ GHz and $f = 8$ GHz. Note from (9) that higher frequencies necessitate a larger number of elements P since the Bessel functions approach zero slower as m increases. So in our application, the upper frequency $f = 8$ GHz in the band of operation sets the smallest number equal to $P = 97$ which meets the approximation for $r = 24$ cm.

4. THE SPATIAL-TEMPORAL INDOOR PROPAGATION CHANNEL

The *array impulse response* $h(t,\theta)$ models the spatial-temporal indoor propagation channel. It is simply the impulse response $h(t)$ in (1) augmented to characterize each multipath k not only by the delay τ_k and the complex-amplitude α_k, but also by the arrival angle ϕ_k:

$$h(t,\theta) = \sum_{k=0}^{K-1} \alpha_k \delta(t-\tau_k,\ \theta-\phi_k). \tag{11}$$

Accordingly, the approach to recover $h(t)$ from the frequency response $H(f)$ through the IDFT in (3) also applies to recover $h(t,\theta)$ from the conventional array frequency response $H(f,\theta)$:

$$h(t,\theta) = \sum_{l=0}^{B/\Delta f} H(f,\theta)e^{j2\pi ft}. \tag{12}$$

The unit array impulse response centered at ($t = 100$ nanoseconds, $\theta = 180^\circ$) appears in Figure 3(a) for the conventional beamformer. The joint f and θ dependence inherent to the phase in (5) generates intractable sidelobes in $h(t,\theta)$ whose zero-crossings in turn vary jointly in the t and θ domains, precluding linear filtering techniques to suppress them.

Likewise, the frequency-invariant array impulse response can be recovered by replacing $H(f,\theta)$ in (12) instead with $\hat{H}(f,\theta)$:

$$h(t,\theta) = \underbrace{\sum_{l=0}^{B/\Delta f} H(f)e^{j2\pi ft}}_{h(t)} \cdot \underbrace{\sum_{m=-(P-1)/2}^{(P-1)/2} e^{jm(\theta+\phi_k)}}_{\hat{h}(\theta)}. \tag{13}$$

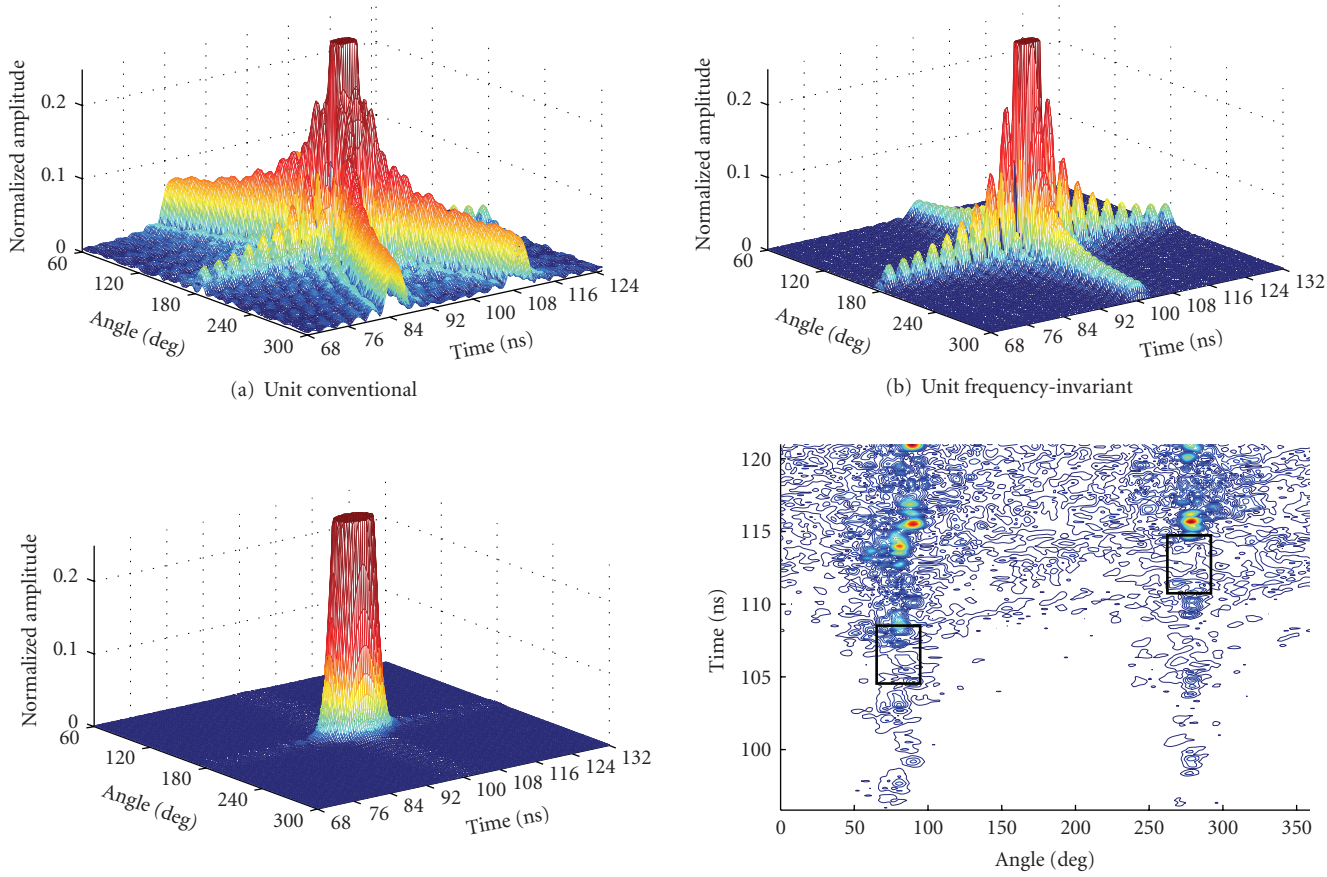

(a) Unit conventional

(b) Unit frequency-invariant

(c) Unit filtered frequency-invariant

(d) Measured filtered frequency-invariant

FIGURE 3: The array impulse response.

Rearranging terms above reveals that $h(t, \theta)$ can be separated into temporal and spatial impulse responses $h(t)$ and $\hat{h}(\theta)$; moreover, each is composed from a finite number of sinusoids and so viable to simple windowing techniques in suppression of the sidelobes. Figures 3(b), 3(c) illustrate the unit array impulse response for the frequency-invariant beamformer and the filtered response using a Kaiser window in both the t and θ dimensions. While superresolution techniques [14] show a significant improvement over the conventional IDFT techniques for smaller bandwidths, the authors in the cited work witnessed no such improvement for bandwidths in excess of 0.2 GHz, those considered in this study. Moreover, such computationally intensive techniques are prohibitive when processing $P \times (B/\Delta f + 1)$ points.

4.1. Time-of-flight and angle-of-flight estimation

The *kurtosis* measure has been recently employed in an effective thresholding technique to detect the time-of-flight from the impulse response [23]. The key strength of this measure lies in its channel invariance, enabling application of the system with no prior knowledge of the environment. In theory, it indicates the Gaussian unlikeness of a window $w[t]$ centered at t when its value defined as

$$\kappa(w[t]) = \frac{E(w^4[t])}{E^2(w^2[t])} \tag{14}$$

exceeds 3. Under the fair assumption of Gaussian noise in the channel [24], the presence of a signal is determined by computing the kurtosis of a fixed-length sliding window originating at the beginning of the impulse response; the first time sample $t = \tau_0$ in the profile at which $\kappa(w[t])$ exceeds the threshold is designated as the leading edge.

The array impulse response was generated with 4800 samples in the temporal dimension spanning 800 nanoseconds, for a resolution of 1/6 nanosecond, and with 180 samples in the angular dimension spanning 360°, for a resolution of 2°. We have adapted the technique to jointly estimate the time and angle-of-flight from the array impulse response by using a two-dimensional window $w[t, \theta]$ instead. Consider a typical frequency-invariant array impulse response for an NLoS scenario in *NIST North* in Figure 3(d). The channel delivers the arrivals in spatial clusters, an observation consistent with [7, 8]. So rather than inefficiently search for (τ_0, ϕ_0) in the two-dimensional space, we first preprocess the

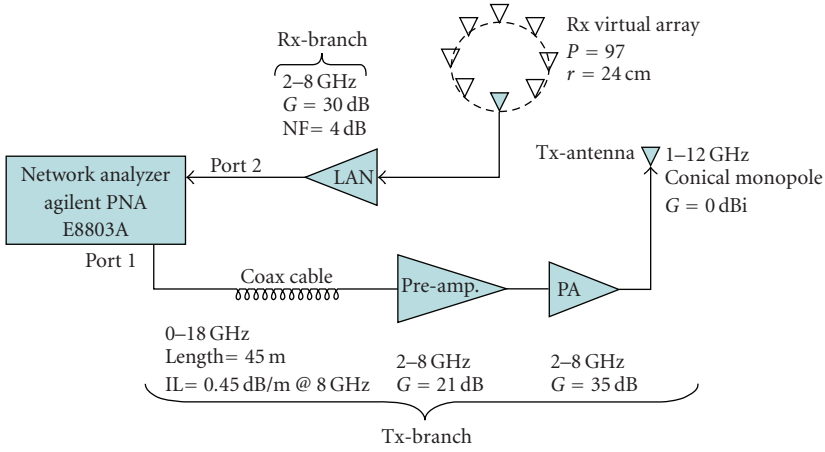

(a) Block diagram

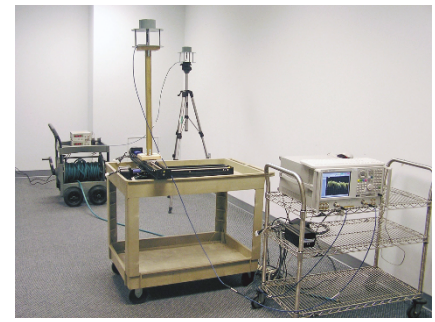

(b) Photograph

FIGURE 4: The measurement system using a vector network analyzer and virtual circular antenna array.

response to isolate a finite number of significant clusters. For each cluster q, we initiate a fixed-dimension window $w[t, \phi^q]$ at the cluster center ϕ^q originating at $t = 0$ and sliding only in the time dimension. Each cluster q elects a candidate leading edge τ^q as the first time sample $t = \tau^q$ in its path when $\kappa(w[t, \theta^q])$ exceeds a threshold. The first cluster is identified as the one with the smallest τ^q. The actual time and angle-of-flight are selected as the sample in the window of the first cluster with the maximum amplitude. Each extraction took less than 1 second on a 400 MHz processor. Through an exhaustive search, the values which minimized the cumulative location error over all the experiments recorded were $33^\circ \times 4$ nanoseconds for the window size and 3.9 for the kurtosis threshold.

5. THE MEASUREMENT SYSTEM

Figure 4 displays the block diagram and photograph of our measurement system. The transmitter antenna is mounted on a tripod while the uniform circular array was realized virtually by mounting the receiver antenna on a positioning table. We sweep the P elements of the array by automatically repositioning the receiver at successive angles θ_i around its perimeter. At each element i, we sweep the discrete frequencies in the 2–8 GHz band. A total channel measurement, comprising the element sweep and the frequency sweep at each element, takes about 24 minutes. To eliminate disturbance due to the activity of personnel throughout the buildings and guarantee a static channel during the complete sweep, the measurements were conducted after working hours.

In the frequency sweep, the vector network analyzer (VNA) emits a series of tones with frequency f at Port 1 and measures the relative amplitude and phase $S^{21}(f)$ with respect to Port 2, providing automatic phase synchronization between the two ports. The synchronization translates to a common time reference for the transmitted and received signals. The long cable enables variable placement of the transmitter and receiver antennas from each other throughout the test area. The preamplifier and power amplifier on the transmit branch boost the signal such that it radiates at approximately 30 dBm from the antenna. After it passes through the channel, the low-noise amplifier (LNA) on the receiver branch boosts the signal above the noise floor of Port 2 before feeding it back.

The $S_i^{21}(f)$-parameter of the network in Figure 4(a) can be expressed as a product of the Tx-branch, the Tx-antenna, the propagation channel, the Rx-antenna, and the Rx-branch

$$\begin{aligned} S_i^{21}(f) &= H_{\text{Tx}}^{\text{bra}}(f) \cdot H_{\text{Tx}}^{\text{ant}}(f) \cdot H_i(f) \cdot H_{\text{Rx}}^{\text{ant}}(f) \cdot H_{\text{Rx}}^{\text{bra}}(f) \\ &= H_{\text{Tx}}^{\text{bra}}(f) \cdot \underbrace{H_{\text{Tx}}^{\text{ant}}(f) \cdot H_{\text{Rx}}^{\text{ant}}(f)}_{H^{\text{ant}}(f)} \cdot H_i(f) \cdot H_{\text{Rx}}^{\text{bra}}(f). \end{aligned} \quad (15)$$

The frequency response of the channel H_i is extracted by individually measuring the transmission responses $H_{\text{Tx}}^{\text{bra}}, H_{\text{Rx}}^{\text{bra}}$, and H^{ant} in advance and de-embedding them from (15). Measuring the characteristics of the antennas on a flat open field with dimensions exceeding 100 m × 100 m reduced ambient multipath to a single-ground bounce which we removed by placing electromagnetic absorbers on the ground between the antennas. To avoid the near-field effects, we separated the antennas by a distance of 1.5 m. Since the receiver does know the relative angle of the transmitter before the location query, it is essential to average out any irregularities in the azimuth radiation pattern to account for this uncertainty and circumvent bias toward any particular angle. This can be achieved through the method in [25] by spatially averaging the antennas through rotation with respect to each other at every ten degrees. Their height was set to 1.7 m (average human height).

Note, in particular, the following implementation considerations:

(i) to account for the frequency-dependent loss in the long cable when operating across such a large bandwidth, we ramped up the emitted power at Port 1 with increasing frequency to radiate from the

Table 1: Experiments conducted in measurement campaign.

Building	Wall material	LoS range (10)	NLoS range (40)
NIST North	Sheet rock/aluminum studs	4.2–23.4 m	2.2–39.1 m max wall#: 9
Child Care	Plaster/wooden studs	2.6–15.3 m	2.8 –32.4 m max wall#: 8
Sound	Cinder block	3.4–43.7 m	2.4–37.5 m max wall#: 10
Plant	Steel	5.2–41.7 m	2.1–44.2 m max wall#: 10

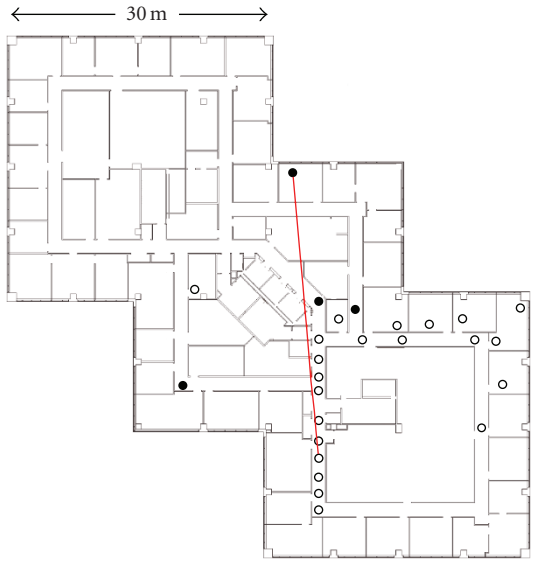

Figure 5: The building plan of *NIST North*.

antenna at approximately 30 dBm across the whole band;

(ii) we removed the LNA from the network in experiments with range below 10 m to protect it from overload and also avert its operation in the nonlinear region;

(iii) to extend the dynamic range of our system, we exploited the configurable test set option of the VNA to reverse the signal path in the coupler of Port 2 and bypass the 12 dB loss associated with the coupler arm. The dynamic range of the propagation channel corresponds to 140 dB as computed through [26] for an IF bandwidth of 1 kHz and an SNR of 15 dB at the receiver.

6. THE MEASUREMENT CAMPAIGN AND RESULTS

The measurement campaign was conducted in four separate buildings on the NIST campus in Gaitherburg, Md, USA each constructed from a dominant wall material varying from sheet rock (easy) to steel (most difficult). Table 1 summarizes the 50 experiments in each building (10 line-of-sight (LoS) and 40 nonline-of-sight (NLoS)), including the maximum number of walls separating the transmitter and the receiver. As an example, consider the floor plan of *NIST North* in Figure 5. The experiments were drawn from two sets of 22 transmitter locations and 4 receiver locations, indicated by the empty and solid circles, respectively, to the end of achieving a uniform distribution in range in both LoS and NLoS conditions. The solid line identifies the experiment with the longest range traversing 9 walls between the transmitter and the receiver.

6.1. Results

For each experiment in the campaign, we compute the *estimated* angle $\hat{\phi} = \phi_0$ and range $\hat{d} = c \cdot \tau_0$, and in turn the estimated location $\hat{\mathbf{x}} = (\hat{d}\cos\hat{\phi}, \hat{d}\sin\hat{\phi})$. The *ground-truth* angle $\overline{\phi}$, range $\overline{d}$, and location $\overline{\mathbf{x}}$ were calculated by pinpointing the coordinates of the transmitter and receiver on site with a laser tape and transferring them to the computer-aided design (CAD) model of each building layout. (There are two sources of human error in the ground-truth measurements: (1) the CAD model was provided by the NIST Plant Division with tolerance of less than 2 cm; (2) the laser tape used gives readings with 1 cm granularity.) The angle error $\phi_e = |\hat{\phi} - \overline{\phi}|$ and range error $d_e = \hat{d} - \overline{d}$ serve as performance measures of the system together with the location error $\mathbf{x}_e = \|\hat{\mathbf{x}} - \overline{\mathbf{x}}\|_2$ encompassing the two jointly. (Due to the irrecoverable delay in estimating the time-of-flight assuming propagation of the signal through walls at the speed of light, the range error is always positive.) Each slot in Table 2 reports the mean values of the three errors $(\mu_{\phi_e}, \mu_{d_e}, \mu_{\mathbf{x}_e})$ across the experiments associated with its cross-labeled scenario. The average pathloss of an experiment can be expressed as [27]

$$\begin{aligned} \mathrm{PL} &= \frac{1}{1 + B/\Delta f} \sum_{l=0}^{B/\Delta f} |H(f)|^2 \\ &= \frac{1}{1 + B/\Delta f} \sum_{l=0}^{B/\Delta f} \left[\frac{1}{P} \sum_{i=0}^{P-1} |H_i(f)|^2 \right]. \end{aligned} \tag{16}$$

Each slot in the table also contains the reference loss PL_0 at $\overline{d}_0 = 1$ m and the exponent γ characterizing the single-slope pathloss model [27]

$$\mathrm{PL}(\overline{d})\,(\mathrm{dB}) = \mathrm{PL}_0 + 10\gamma \log_{10}\left(\frac{\overline{d}}{\overline{d}_0}\right) \tag{17}$$

fit to the PL values (16) of the scenario experiments. Reporting the pathloss for each scenario disassociates the results from our particular transmitter power and receiver sensitivity. The highest pathloss in all the environments

Table 2: Statistical results for experiments $\mu_{\phi_e}(^\circ)$, μ_{d_e} (cm), $\mu_{\mathbf{x}_e}$ (cm), PL_0, γ.

	Building	$B = 0.5$		$B = 1$			$B = 2$			$B = 4$		$B = 6$
		$f_c = 5$	$f_c = 3$	$f_c = 5$	$f_c = 7$	$f_c = 3$	$f_c = 5$	$f_c = 7$	$f_c = 4$	$f_c = 5$	$f_c = 6$	$f_c = 5$
12∗LoS	*NIST North*	2.3, 35	1.9, 17	1.9, 19	2.0, 18	1.3, 12	1.3, 14	1.3, 18	1.0, 12	0.8, 11	0.8, 14	0.6, 9
		109	62	64	65	44	46	48	35	23	36	19
		42, 1.5	41, 1.2	42, 1.5	44, 1.7	47, 1.0	42, 1.4	42, 2.0	41, 1.2	45, 1.3	44, 1.6	44, 1.6
	Child Care	2.7, 41	2.1, 30	2.1, 32	2.2, 33	2.5, 25	1.9, 25	1.5, 24	1.7, 18	1.6, 21	1.4, 22	1.5, 20
		121	66	67	69	257	46	39	38	40	43	38
		43, 2.1	39, 2.2	39, 2.1	41, 2.2	39, 2.0	41, 2.2	40, 2.4	40, 2.0	41, 2.1	42, 2.2	41, 2.1
	Sound	2.8, 57	2.0, 38	2.0, 43	2.1, 47	1.7, 26	1.5, 27	1.3, 23	1.4, 19	1.3, 20	1.1, 23	1.2, 18
		176	97	99	103	67	71	77	61	63	67	61
		39, 2.2	38, 2.6	42, 2.4	44, 2.8	44, 1.6	42, 2.5	42, 2.4	37, 2.2	40, 2.3	41, 2.7	43, 2.9
	Plant	3.1, 74	2.1, 59	2.2, 57	2.0, 61	1.8, 32	1.3, 34	0.9, 30	1.0, 34	0.9, 35	0.8, 34	0.8, 33
		182	105	102	109	71	67	62	61	65	68	64
		38, 1.7	39, 1.6	41, 2.0	39, 2.3	40, 1.3	42, 1.9	41, 1.9	41, 1.7	41, 1.8	42, 2.0	41, 1.7
12∗NLoS	*NIST North*	10.8, 93	7.9, 64	8.3, 64	8.5, 64	6.7, 41	6.0, 42	5.5, 39	3.8, 21	3.9, 29	3.6, 38	3.4, 24
		457	312	327	346	284	274	261	198	188	192	150
		26, 4.5	26, 4.3	26, 4.6	23, 5.0	28, 3.8	26, 4.6	30, 4.2	27, 4.5	29, 4.3	27, 4.5	29, 4.0
	Child Care	16.3, 109	11.2, 76	11.8, 78	12.3, 81	9.9, 47	9.1, 53	8.4, 56	6.5, 38	6.3, 47	6.2, 49	5.5, 45
		464	347	357	368	289	275	247	172	6182	186	159
		13, 6.2	13, 5.7	14, 6.2	12, 7.0	12, 6.2	10, 6.2	8, 7.5	12, 5.6	13, 6.3	15, 6.5	13, 6.7
	Sound	27.2, 253	17.2, 189	20.9, 212	23.5, 224	17.0, 169	16.8, 172	18.8, 177	16.9, 131	15.7, 139	15.5, 152	15.2, 128
		1122	917	926	952	756	772	830	652	689	676	656
		28, 5.4	28, 4.7	31, 5.2	32, 5.4	30, 4.8	31, 5.2	35, 5.4	27, 5.1	32, 5.2	32, 5.0	33, 5.1
	Plant	79.2, 611	37.0, 475	36.6, 467	35.2, 482	29.8, 454	27.7, 472	24.5, 489	24.2, 422	23.7, 436	23.9, 456	23.2, 419
		2313	1372	1361	1354	1111	1134	1143	1006	1043	1052	995
		48, 1.5	50, 1.6	52, 1.7	53, 1.8	50, 1.5	52, 1.7	54, 1.8	48, 1.7	51, 1.7	52, 1.7	53, 1.6

(NLoS in *Child Care* and *Sound*) can be computed as 114 dB at the longest range of 45 m, leaving a margin of 26 dB in the total dynamic range of 140 dB of our system to ensure accurate range and angle estimation even in the most challenging experiments.

Figure 6(a) illustrates the angle, range, and locations errors multiplexed on the ordinate versus the ground-truth range for the line-of-sight experiments in *NIST North* for ($B = 6$ GHz, $f_c = 5$ GHz). The color of the point represents the pathloss (dB) in reference to the bar. The strength of the first arrival decreases with range, but can be detected without degrading the system performance so long as it remains above the receiver sensitivity. It follows that no obvious correlation exists between error and ground-truth range in line-of-sight conditions. The angle error lies within 2°, the range error within 11 cm, and the location error within 54 cm. The mean errors ($\mu_{\phi_e}, \mu_{d_e}, \mu_{\mathbf{x}_e}$) of each scenario from Table 2 also appears on each plot as a hollow square to highlight the trend in parameter variation. Performance improves significantly with increasing bandwidth, but at diminishing returns. $\mu_{\mathbf{x}_e}$ drops from 109 to 62 cm from $B = 0.5$ to 1 GHz, but only from 23 to 19 cm from $B = 4$ to 6 GHz. This phenomenon holds true throughout all LoS and NLoS scenarios in all buildings as a consequence of the relationship $\tau_z = 1/B$ (see Section 2) and in turn $d\tau_z/\mathrm{dB} = -1/B^2$, hence the same increment in bandwidth dB at a higher operating bandwidth B results in a smaller decrement in the pulse width which controls the resolution performance of the system. So once the paths are resolvable, increasing the bandwidth further offers no improvement. The LoS experiments in the other three buildings exhibit similar behavior as in *NIST North*.

The plots in Figures 6(b)–6(d) display the nonline-of-sight scenarios in *NIST North*, *Child Care*, and *Sound* for ($B = 6$ GHz, $f_c = 5$ GHz). While remarkably worse than in the LoS experiments, in *NIST North* $\mu_{\phi_e} = 3.4°$ (1.8% as a percentage of the maximum angle error of 180°), $\mu_{d_e} = 24$ cm (0.6% as a percentage of the maximum ground-truth range), and $\mu_{\mathbf{x}_e} = 150$ cm. Note in passing that in nonline-of-sight conditions we have observed that the strongest arrival comes from the direction of the door(s) when placing the receiver in a room and from the direction of the corridor(s) when placing it in a hallway [1]. Its angle is then random and uniformly distributed between 0° and 360° and so too would be the angle error if estimating the arrival angle as that of the strongest arrival rather than the first arrival

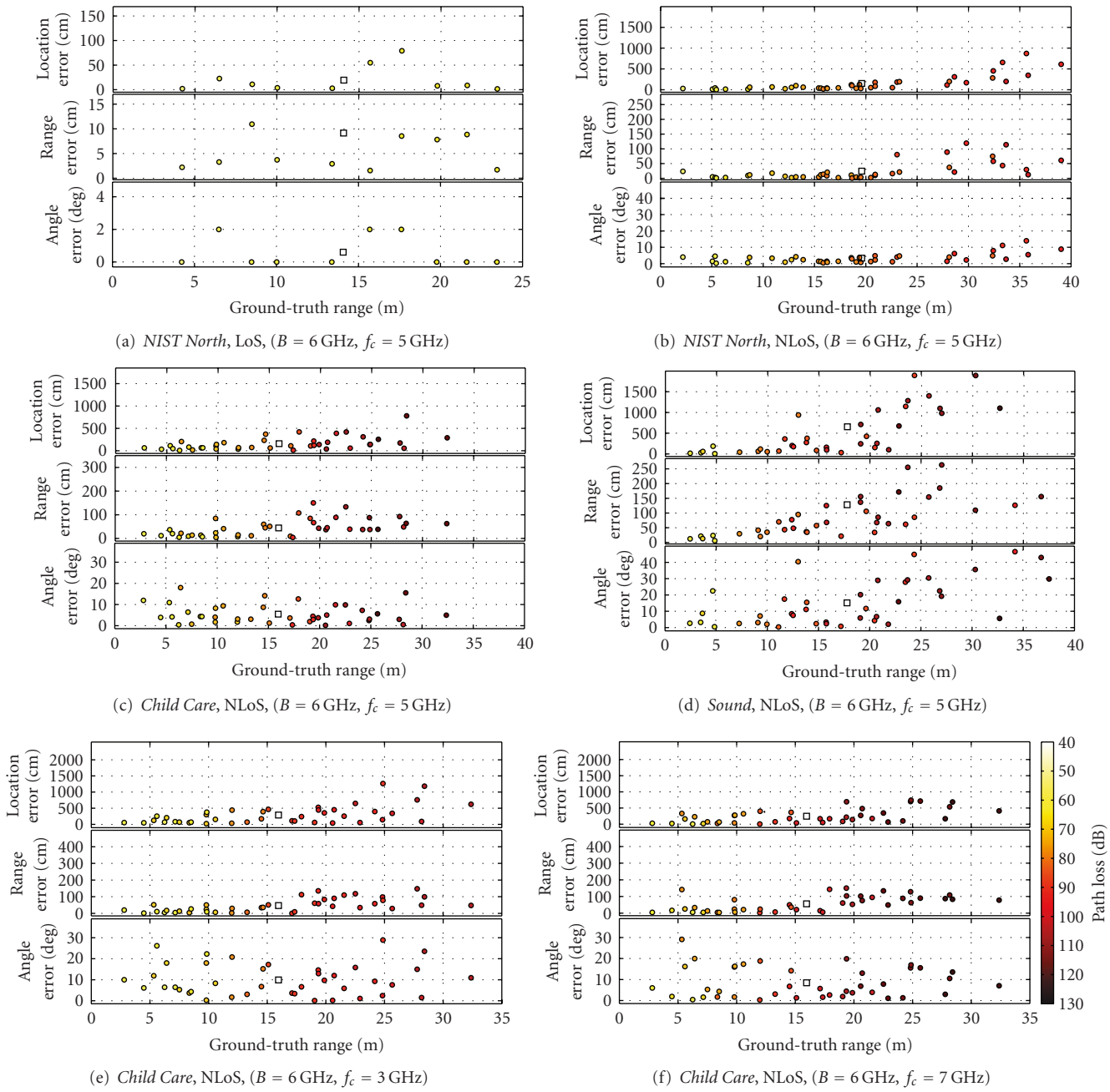

(a) *NIST North*, LoS, ($B = 6$ GHz, $f_c = 5$ GHz)

(b) *NIST North*, NLoS, ($B = 6$ GHz, $f_c = 5$ GHz)

(c) *Child Care*, NLoS, ($B = 6$ GHz, $f_c = 5$ GHz)

(d) *Sound*, NLoS, ($B = 6$ GHz, $f_c = 5$ GHz)

(e) *Child Care*, NLoS, ($B = 6$ GHz, $f_c = 3$ GHz)

(f) *Child Care*, NLoS, ($B = 6$ GHz, $f_c = 7$ GHz)

Figure 6: Angle, range, and location errors versus ground-truth range.

when lacking information on its arrival time. The mean error triplet increases in the more challenging buildings to ($\mu_{\phi_e} = 5.5^\circ$, $\mu_{d_e} = 45$ cm, $\mu_{\mathbf{x}_e} = 159$ cm) in *Child Care* and ($\mu_{\phi_e} = 15.2^\circ$, $\mu_{d_e} = 128$ cm, $\mu_{\mathbf{x}_e} = 656$ cm) in *Sound*; considering that the signal traverses up 10 walls in these two buildings, the results fare quite well. As explained in Section 2, each wall interaction distorts the leading edge both in time and angle-of-flight, placing a physical limit on the system no matter the dynamic range. The system performs poorly in *Plant*, where for the most part the angle error is distributed uniformly between 0° and 40° independent of the range, and the range error lies below 500 cm only up to 15 m, clearly manifesting the impenetrable properties of metal by the direct path.

In varying center frequency for fixed bandwidths of $B = \{1, 2, 4\}$ GHz, Table 2 confirms that the lower bands penetrate the materials better [6, 28] through the smaller mean range errors for most nonline-of-sight scenarios in *NIST North*, *Child Care*, and *Sound*. The improvements are less noticeable in *NIST North* compared to the other two since the thin sheet rock walls have favorable electromagnetic properties for which the first arrival is equally detectable on both bands even at long ranges. On the other hand, the upper bands offer better angular resolution (see Section 3)

and in turn yield smaller mean angle errors for the most part. The two opposing phenomena in the lower and upper bands yield mixed, but comparable, results in terms of mean location error across the four buildings, and so we conclude that there is no clear optimal center frequency of operation in this regard. Figures 6(e) and 6(f) illustrate these trends in comparing lower $f_c = 3$ GHz to upper $f_c = 7$ GHz for fixed $B = 2$ GHz in *Child Care*, where the mean range error increases 9 cm, the mean angle error decreases 1.5°, and in this case the mean location error decreases 42 cm.

7. CONCLUSIONS

Our nominal ranging and bearing system at 6 GHz bandwidth and 5 GHz center frequency delivers a mean angle error of 1° and a mean range error of 20 cm in line-of-sight conditions up to a range of 45 m throughout all four buildings tested. The angle error increases to 3.4°, 5.5°, and 15.2° and the range error increases to 24 cm, 45 cm, and 128 cm for sheet rock, plaster, and cinder block wall materials, respectively, in nonline-of-sight conditions; the system ranges within 35° and 500 cm up to 15 m in the steel building, but the performance degrades rapidly thereafter. In comparing subbands with 2 GHz bandwidth centered at 3 GHz and 7 GHz, respectively, the lower band yields up to 8 cm smaller mean range error since lower frequencies penetrate walls better, but the upper band yields up to 1.2° smaller mean angle error since higher frequencies offer better angular resolution.

REFERENCES

[1] C. Gentile, S. Martinez-Lopez, and A. Kik, "A comprehensive spatial-temporal propagation model for the ultra-wideband spectrum 2–8 GHz," submitted to *IEEE Transactions on Antennas and Propagation*.

[2] A. F. Molisch, "Ultrawideband propagation channels-theory, measurement, and modeling," *IEEE Transactions on Vehicular Technology*, vol. 54, no. 5, pp. 1528–1545, 2005.

[3] Z. Irahhauten, H. Nikookar, and G. J. M. Janssen, "An overview of ultra wide band indoor channel measurements and modeling," *IEEE Microwave and Wireless Components Letters*, vol. 14, no. 8, pp. 386–388, 2004.

[4] J.-Y. Lee and R. A. Scholtz, "Ranging in a dense multipath environment using an UWB radio link," *IEEE Journal on Selected Areas in Communications*, vol. 20, no. 9, pp. 1677–1683, 2002.

[5] B. Denis, J. Keignart, and N. Daniele, "Impact of NLOS propagation upon ranging precision in UWB systems," in *Proceedings of IEEE Conference on Ultra Wideband Systems and Technologies*, pp. 379–383, Reston, Va, USA, November 2003.

[6] C. Gentile and A. Kik, "A comprehensive evaluation of indoor ranging using ultra-wideband technology," *EURASIP Journal on Wireless Communications and Networking*, vol. 2007, Article ID 86031, 10 pages, 2007.

[7] R. J.-M. Cramer, R. A. Scholtz, and M. Z. Win, "Evaluation of an ultra-wide-band propagation channel," *IEEE Transactions on Antennas and Propagation*, vol. 50, no. 5, pp. 561–570, 2002.

[8] Q. H. Spencer, B. D. Jeffs, M. A. Jensen, and A. L. Swindlehurst, "Modeling the statistical time and angle of arrival characteristics of an indoor multipath channel," *IEEE Journal on Selected Areas in Communications*, vol. 18, no. 3, pp. 347–360, 2000.

[9] A. S. Y. Poon and M. Ho, "Indoor multiple-antenna channel characterization from 2 to 8 GHz," in *Proceedings of IEEE International Conference on Communications (ICC '03)*, vol. 5, pp. 3519–3523, Anchorage, Alaska, USA, May 2003.

[10] S. Venkatesh, V. Bharadwaj, and R. M. Buehrer, "A new spatial model for impulse-based ultra-wideband channels," in *Proceedings of the 62nd IEEE Vehicular Technology Conference (VTC '05)*, vol. 4, pp. 2617–2621, Dallas, Tex, USA, September 2005.

[11] K. Haneda, J.-I. Takada, and T. Kobayashi, "Cluster properties investigated from a series of ultrawideband double directional propagation measurements in home environments," *IEEE Transactions on Antennas and Propagation*, vol. 54, no. 12, pp. 3778–3788, 2006.

[12] H. Hashemi, "The Indoor radio propagation channel," *Proceedings of the IEEE*, vol. 81, no. 7, pp. 943–968, 1993.

[13] A. Muqaibel, A. Safaai-Jazi, A. Bayram, A. M. Attiya, and S. M. Riad, "Ultrawideband through-the-wall propagation," *IEE Proceedings on Microwaves, Antennas, & Propagation*, vol. 152, no. 6, pp. 581–588, 2005.

[14] X. Li and K. Pahlavan, "Super-resolution TOA estimation with diversity for indoor geolocation," *IEEE Transactions on Wireless Communications*, vol. 3, no. 1, pp. 224–234, 2004.

[15] C. A. Balanis, *Antenna Theory: Analysis and Design*, John Wiley & Sons, New York, NY, USA, 2nd edition, 1997.

[16] T. B. Vu, "Side-lobe control in circular ring array," *IEEE Transactions on Antennas and Propagation*, vol. 41, no. 8, pp. 1143–1145, 1993.

[17] D. K. Cheng, "Optimization techniques for antenna arrays," *Proceedings of the IEEE*, vol. 59, no. 12, pp. 1664–1674, 1971.

[18] N. Goto and Y. Tsunoda, "Sidelobe reduction of circular arrays with a constant excitation amplitude," *IEEE Transactions on Antennas and Propagation*, vol. 25, no. 6, pp. 896–898, 1977.

[19] E. Doron and M. A. Doron, "Coherent wideband array processing," in *Proceedings of IEEE International Conference on Speech, Acoustics and Signal Processing (ICASSP '92)*, vol. 2, pp. 497–500, San Francisco, Calif, USA, March 1992.

[20] C. P. Mathews and M. D. Zoltowski, "Performance analysis of the UCA-ESPRIT algorithm for circular ring arrays," *IEEE Transactions on Signal Processing*, vol. 42, no. 9, pp. 2535–2539, 1994.

[21] S. C. Chan and H. H. Chen, "Uniform concentric circular arrays with frequency-invariant characteristics—theory, design, adaptive beamforming and DOA estimation," *IEEE Transactions on Signal Processing*, vol. 55, no. 1, pp. 165–177, 2007.

[22] M. Wax and J. Sheinvald, "Direction finding of coherent signals via spatial smoothing for uniform circular arrays," *IEEE Transactions on Antennas and Propagation*, vol. 42, no. 5, pp. 613–620, 1994.

[23] I. Guvenc and Z. Sahinoglu, "Threshold selection for UWB TOA estimation based on kurtosis analysis," *IEEE Communications Letters*, vol. 9, no. 12, pp. 1025–1027, 2005.

[24] I. Guvenc and Z. Sahinoglu, "Threshold-based TOA estimation for impulse radio UWB systems," in *Proceedings of IEEE International Conference on Ultra-Wideband (ICU '05)*, vol. 2005, pp. 420–425, Zurich, Switzerland, September 2005.

[25] S. Zwierzchowski and P. Jazayeri, "A systems and network analysis approach to antenna design for UWB communications," in *Proceedings of IEEE Antennas and Propagation Society International Symposium (APS '03)*, vol. 1, pp. 826–829, Columbus, Ohio, USA, June 2003.

[26] J. Keignart and N. Daniele, "Subnanosecond UWB channel sounding in frequency and temporal domain," in *Proceedings of IEEE Conference on Ultra Wideband Systems and Technologies (UWBST '02)*, pp. 25–30, Baltimore, Md, USA, May 2002.

[27] S. S. Ghassemzadeh, L. J. Greenstein, T. Sveinsson, A. Kavčić, and V. Tarokh, "UWB delay profile models for residential and commercial indoor environments," *IEEE Transactions on Vehicular Technology*, vol. 54, no. 4, pp. 1235–1244, 2005.

[28] D. Cassioli, A. Durantini, and W. Ciccognani, "The role of path loss on the selection of the operating bands of UWB systems," in *Proceedings of the 15th IEEE International Symposium on Personal, Indoor and Mobile Radio Communications (PIMRC '04)*, vol. 4, pp. 2787–2791, Barcelona, Spain, September 2004.